Materials Chemistry and Physics 136 (2012) 990–998

Contents lists available at SciVerse ScienceDirect

Materials Chemistry and Physics

journal homepage: www.elsevier.com/locate/matchemphys

XAFS and TEM studies of the structural evolution of yttrium-enriched oxides in nanostructured ferritic alloys fabricated by a powder metallurgy process

P. He [a,*], T. Liu [b], A. Möslang [a], R. Lindau [a], R. Ziegler [a], J. Hoffmann [a], P. Kurinskiy [a], L. Commin [a], P. Vladimirov [a], S. Nikitenko [c], M. Silveir [c]

[a] Institute for Applied Materials-Applied Materials Physics, Karlsruhe Institute of Technology, Eggenstein-Leopoldshafen, PO Box 3640, 76021 Karlsruhe, Germany
[b] Institute for Synchrotron Radiation, Karlsruhe Institute of Technology, Eggenstein-Leopoldshafen, Germany
[c] European Synchrotron Radiation Facility, Grenoble, France

HIGHLIGHTS

- The structural evolution of yttrium-enriched oxides was analyzed by XAFS Y K-edge.
- 10%–14% of the 0.3 wt. % Y_2O_3 dissolves into the matrix after 24 h of MA.
- The formation of a new Y–Cr–O/Y_2O_3 phase is observed in compacted 0% Ti alloys.
- A Y–Ti–O/Y_2O_3 phase in the alloys containing Ti is confirmed by EXAFS and EDX.
- Ti exhibits an evident influence in the consolidation process rather than in the MA.

ARTICLE INFO

Article history:
Received 10 May 2012
Received in revised form
7 August 2012
Accepted 20 August 2012

Keywords:
ODS ferritic alloy
Y-enriched oxide
XAFS
TEM
Mechanical alloying

ABSTRACT

The speciation and structural evolution of nanoscale yttrium-enriched oxides in numerous reduced activation oxide dispersion strengthened (ODS) ferritic steels have been investigated by X-ray absorption fine structure (XAFS) spectroscopy (including X-ray absorption near-edge structure and extended X-ray absorption fine structure) and transmission electron microscopy (TEM). The local structure and speciation of Y-enriched oxides during the fabrication process have been traced by Yttrium (Y) K-edge XAFS in fluorescence mode for both mechanical alloyed (MA) powders and compacted ODS alloys. After 24 h of milling, only 10%–14% of the initially added 0.3 wt. % Y_2O_3 dissolves into the steel matrix and titanium (Ti) exhibits a minor influence on the Y solid solution during the MA. The EXAFS analysis for compacted ODS alloys indicates the formation of new Y-enriched oxides rather than initial Y_2O_3. The presence of Y–Cr–O/Y_2O_3 has been confirmed by EXAFS and energy dispersed X-ray spectroscopy (EDX) elemental mapping in the compacted ODS alloy without Ti, while Y–Ti–O/Y_2O_3 was observed in Ti-containing (0.2–0.4 wt. %) ODS alloys. The addition of Ti exhibits an evident influence on the consolidation process rather than in the MA.

1. Introduction

The rapidly growing demand for new energy sources has rekindled the worldwide motivation to develop innovative energy systems. The development of appropriate materials for these systems has been recognized as a most challenging task. Reduced activation ferritic ODS steels are presently considered to be promising candidates for the 4th generation (Generation IV) of nuclear reactors [1], future fusion reactors, as well as accelerator-driven systems for nuclear waste incineration due to their favorable mechanical properties, superior resistance under neutron irradiation, good coolant compatibility, and technical maturity. Besides nuclear applications, ODS steels are prospective candidates for various high-tech applications, including CO_2-free production of hydrogen, solar thermal energy conversion, or generally high temperature applications in corrosive environments.

In fusion reactors, in particular, high energy neutrons (14 MeV) produce large amounts of point defects, helium (He) by transmulation with a concentration up to 2000 appm and atomic displacements up to 200 dpa. Such a harsh environment results in severe materials degradation in terms of irradiation hardening, irradiation embrittlement, and He-embrittlement. A recent experiment has shown that the nanoscale oxides and grain structure in

* Corresponding author. Tel.: +49 721 608 22908; fax: +49 721 608 24567.
E-mail address: pei.he@kit.edu (P. He).

0254-0584/$ – see front matter © 2012 Elsevier B.V. All rights reserved.
http://dx.doi.org/10.1016/j.matchemphys.2012.08.038

MA957 undergo minor changes after neutron irradiation between 500 °C and 700 °C up to 100 dpa [2]. In principle, the irradiation damage resistance of ODS steels derives from their high sink densities, including stabilized dislocation structures and a large number of fine oxide particles by the addition of 0.25–0.5 wt. % yttria (Y_2O_3) [3].

Conventional melt processing techniques cannot be applied to fabricate ODS steels due to the extremely low solubility limit of yttrium (Y) in Fe and the high melting point of Y_2O_3 (2410 °C). The common approach to ODS alloy fabrication is the powder metallurgy route, consisting of mechanical alloying (MA) followed by either hot extrusion (HE) or hot isostatic pressing (HIP). The main function of MA is to break up the chemical bonds in the Y_2O_3 particles and to force the Y and O to incorporate into the steel matrix. The degree of dissolution, the speciation, and the local structure of Y are of particular significance for the optimization of the MA parameters. These factors also influence the subsequent formation of Y–X–O (X = Ti, Al, Cr,…) ternary oxides during the consolidation process, which strongly affects the mechanical properties of the ODS alloys.

In 1993, Ukai et al. [4] first recognized the influence of dissolved Ti on the refinement of Y_2O_3 precipitates, attributing this to $TiO_2 + Y_2O_3 \rightarrow Y_2TiO_5$ reactions. Cubic Y_2O_3 particles were found in EUROFER-ODS without Ti [5]. Near stoichiometric complex oxides with a typical sizes larger than 10 nm, such as Y_2TiO_5 and Y_2TiO_7, were observed in Ti-containing ODS steels by high resolution TEM [6]. Atom probe tomography (APT) [7,8] provided chemical information on the non-equilibrium Y–Ti–O ultrafine particles, with high Ti/Y ratios (typically 2–4/1) and high (Y + Ti)/O ratios greater than 1 (typically 1.25–15/1). These ultrafine Y, Ti, O-enriched particles with a size of about 2 nm in diameter are different from the complex oxides $Y_2Ti_2O_7$ and Y_2TiO_5. These discordant observations can be partly due to the fact that there is a range of different oxide particles in ODS steels.

Both TEM and APT are local probes and measure an extremely limited area. Consequently, the results obtained by these techniques may, in some cases, be hard to transfer to the whole alloy. It is more challenging for ODS steels because of the low concentration of Y_2O_3 and the poor crystallinity of MA powders. In order to address this issue, X-ray absorption fine structure (XAFS) spectroscopy combined with advanced synchrotron sources are employed to study the evolution of yttrium oxides during the fabrication process. XAFS provides a practical and simple way to study elements of minor and even trace contents, giving a unique and direct measurement of chemical and physical states of dilute species over the whole sample. The X-ray absorption spectrum is typically divided into two regimes: X-ray absorption near-edge structure (XANES) and extended X-ray absorption fine structure (EXAFS). These provide complementary structural information. XANES is strongly sensitive to the formal oxidation state and coordination chemistry of the absorbing atom, and EXAFS is usually used to determine the distances, coordination number, and speciation of the neighbors of the absorbing atom.

In this paper, a detailed XAFS study of several 13.5% Cr ODS steels is presented. Our aim is to reveal the local environment of the trace Y element in ODS steels and study the influence of the amount of Ti after MA and after consolidation. Such an analysis helps to determine whether and how much Y_2O_3 is dissolved during the MA and provides clues to new nanoscale Y-enriched oxides during the consolidation. A joint application of XAFS and TEM is aimed not only at a better understanding of the structure–property correlation, but also at the optimization of the chemical and physical processes involved in the fabrication. Another goal of this study is to evaluate the suitability of the XAFS technique for being a powerful tool for the investigation of ODS alloys.

2. Experimental

2.1. Material

The ODS steel powders were produced by mechanical alloying of pre-alloyed Fe-13.5Cr-2W powders (in wt. %) with 0.3 wt. % Y_2O_3 and 0–0.4 wt. % TiH_2 powders. The details of the fabrication process were described elsewhere [9]. Briefly, the MA was performed in a ZOZ Attritor, under a highly pure hydrogen atmosphere. Then the milled powders were filled in specially designed stainless steel capsules (18Cr8Ni) and degassed at 400 °C for 4 h in vacuum. Afterward the canned powders were consolidated by HIP for 2.5 h at 1150 °C under a pressure of 100 MPa followed by annealing at 1050 °C for 2 h. The nominal composition and other experimental details are summarized in Table 1. The MA steel powders together with the compacted steels were investigated by XAFS. Commercially available yttria powders and Y metal foil were used as standards. The crystal structure of the pure yttria powders was examined by an X-ray diffractometer (Seifert MZ IV diffractometer) using nickel-filtered Cu Kα1/2 radiations. The diffraction data were collected over a 2θ range of 10°–120°, with a step width of 0.04°.

2.2. TEM

The samples for the TEM study were mechanically ground to 130 μm in thickness. Discs of 3 mm in diameter were punched from these thin slices and then electro-polished in a TENUPOL-5 device using 20% H_2SO_4 + 80% CH_3OH as electrolyte. The samples were further cleaned with an argon ion beam using a Precise Ion Polishing System (PIPS).

The investigations were performed using a FEI Tecnai 20 F (200 kV, field emission gun) microscope equipped with a high-angle annular dark field (HAADF) detector. The energy dispersed X-ray spectroscopy (EDX) experiments were performed in the scanning TEM (STEM) mode and the EDX spectra were recorded using an EDAX Si/Li detector with an ultra-thin window. The electron beam used for imaging and analysis has a probe size of 1.0–1.2 nm.

2.3. XAFS

The XAFS measurements were performed on the bending magnet line of sector 26A (BM26A) at the European Synchrotron Radiation Facility (ESRF). The beam from the bending magnet source passes through a monochromator, which is used to select the X-ray energy. Harmonics are eliminated by a flat mirror installed downstream. In transmission mode, the intensities of the incident beam and the transmitted beam were collected by two ionization chambers, while in fluorescence mode the fluorescence intensity was recorded by a multi-element Ge detector. All data for

Table 1
List of alloy composition, fabrication parameters and measuring mode of XAFS, composition is given in wt. %.

Sample	Composition	Measurement	Remarks
Reference	Y foil	Transmission	Purchased
	Y_2O_3		
MA steel powders	0Ti	Fluorescence	MA: 24 h; H_2;
Fe-13.5Cr-2W	0.2Ti		Ball-to-powder ratio = 10:1
	0.3Ti		
	0.4Ti		
Compacted samples	0Ti		MA + HIP + HT: 1150 °C,
Fe-13.5Cr-2W	0.2Ti		100 MPa, 2.5 h (HIP);
	0.3Ti		1050 °C, 2 h, vacuum (HT)
	0.4Ti		

the MA powders and compacted steel samples were collected in fluorescence mode due to the low concentration of Y. A Y metal foil with a thickness of 25 μm was measured for energy calibration. Pure yttria powders were ground, mixed with boron nitride (BN) powders, pressed into pellets, and measured in transmission mode. All the measurements were performed at Y K-edge (17.038 keV) at room temperature. For each alloy sample, 5–10 energy scans were collected and averaged to improve the statistics.

2.4. Data evaluation

The XAFS data were analyzed by the code WINXAS [10] according to a standard procedure. The procedure includes the conversion of the raw data to μ(E) spectra, background subtraction, normalization, transformation from energy space to wave-vector (k) space, spline function fit, Fourier transforming, filtering, and fitting. In the background subtraction, a linear function and a two-order polynomial function were used for the fit of the pre-edge and post-edge regions. The threshold energy, E_0, was determined as the energy of the maximum derivative of $\mu(E)$. The transformation into k space was performed on the spectra by using the formula $k = \sqrt{2m(E-E_0)/\hbar^2}$, where m is the mass of the electron and $\hbar$ is Planck's constant. The EXAFS function $\chi(k)$ was obtained by extracting the background simulated by a spline function at the spectra in k space. Then, the Fourier transform of $k^3\chi(k)$ was calculated with a Bessel window function, resulting in a direct correlation with the radial distribution function in real space. The fitting of the first two or three coordination shells was done in real space by using the phaseshift and backscattering amplitude extracted from model compounds using FEFF.

The basic EXAFS equation is [11].

$$\chi(k) = \sum_j \frac{N_j S_0^2 F_j(k) e^{-2R_j/\lambda(k)} e^{-2k^2\sigma_j^2}}{kR_j^2} \sin[2kR_j + \delta_j(k)] \quad (1)$$

In Eq. (1), the sine function describes the interference pattern. $F_j(k)$ is the backscattering amplitude, which is element specific. S_0^2 is an amplitude reduction factor representing many-body effects, which was experimentally determined by the fit to the model compounds. The exponential term containing the mean free path λ of the photoelectrons accounts for the finite lifetime of the excited state. Using this equation, some physical parameters can be extracted by fitting the XAFS data: (1) R, the distance between the absorber and the neighboring atoms; (2) N, the coordination number of the neighboring atom; (3) σ^2, the mean-square disorder of the neighbor distance or the fluctuation in R_j. To extract these important parameters, an accurate determination of the scattering amplitude $F_j(k)$ and the phase shifts $\delta_j(k)$ is necessary, which were usually calculated by FEFF code using the crystallographic data from model compounds [11].

3. Results

3.1. XRD

The pure yttria powders were provided by Alfa Aesar and have a size 25–50 nm. They were used as an essential reference for the XAFS data evaluation. c-Y_2O_3 (cubic, the space group Ia3) is thermodynamically stable up to 2330 °C, when it transforms into a hexagonal (space group $P\bar{3}$ m1) phase or a fluorite-type face centered cubic form (space group Fm3m) [12]. Its phase stability is also strongly dependent on the particle size. The m-Y_2O_3 (monoclinic, space group C2/m) and c-Y_2O_3 may coexist if the particle size decreases to nanoscale owing to the increasing importance of surface effects [13]. The commercial Y_2O_3 powders were characterized by XRD, as shown in Fig. 1. In comparison with the JCPDS data card, the experimental data is in good agreement with the body centered cubic phase (pattern number is 00-041-1105, Ia3). The main peaks are perfectly indexed with the exception of two small peaks at 2θ of 27.6° and 32.36°. The inconsistency at such angles probably results from impurities in the yttria powders.

3.2. XANES

3.2.1. Powders

The XAFS investigations of ODS steels have been focused on the Y K-edge because Y is the major constituent of the nanoscale particles. The absorption edge, E_0 lying around 17.038 keV, does not interfere with the other elements in the steel (Fe: 7.112 keV; Cr: 5.989 keV; W: 69.525 keV; Ti: 4.966 keV) [14]. The K-edge in XANES, as indicated by arrow A in Fig. 2, is sensitive to the oxidation state of Y. A higher valence of the absorber usually has an absorption edge shifting toward higher energy. The normalized XANES spectra for four MA powders with the two references, Y foil and Y_2O_3, are compared. Y_2O_3 features separated peaks (B and C) of higher intensities and a shift toward higher energy. For MA powders, the shoulder C above the main peak B is indistinct and all the spectra seem identical, which suggests that all the Y in the various MA powders have similar chemical environments, and that the influence of Ti is trivial. The smeared-out peak C indicates a structure without long range ordering in nano Y_2O_3 particles [15]. The chemical shift of the MA powders lies between Y metal and Y_2O_3, implying that there is a portion of the Y in the metallic state.

In order to resolve the relative ratio of metallic Y over total Y, linear combination fits of the normalized XANES for MA powders were performed using Y metal and Y_2O_3. The fitting result is satisfactory, as shown in Fig. 3a. An alternative model was tried by replacing Y_2O_3 with a compacted sample with 0.4% Ti. A good agreement is observed in Fig. 3b and the relative ratio $Y_{dissolve}/Y_{total}$ in weight percentage can be obtained. The $Y_{dissolve}/Y_{total}$ ratio for all the MA powders is summarized in Table 2. The metallic Y component lies between 10.2% and 13.7% and varies slightly with the minor changes in the amount of Ti. The metallic Y component arises from either Fe–Y solid solution or pure Y. Because of the tiny difference of charge transfer for Y–Y and Y–Fe, their similar chemical shifts cannot be distinguished by XANES. Driven by high energy milling, part (not all) of the Y_2O_3 may be reduced in the reducing atmosphere (H_2). Another possibility is that atomic Y diffuses into the Fe lattice and forms a substitutional alloy.

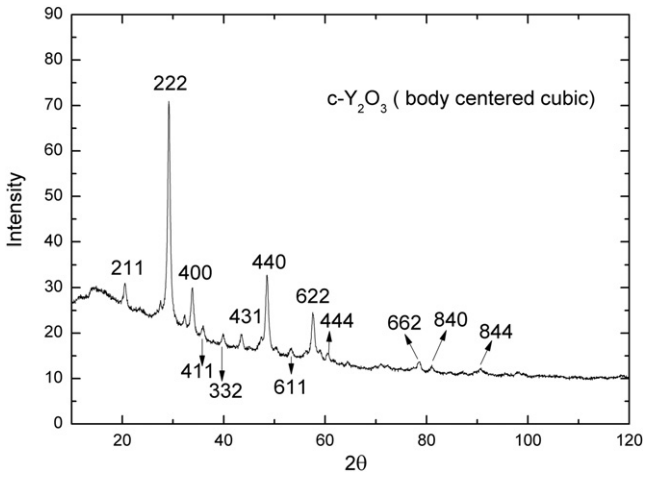

Fig. 1. XRD pattern of pure cubic Y_2O_3.

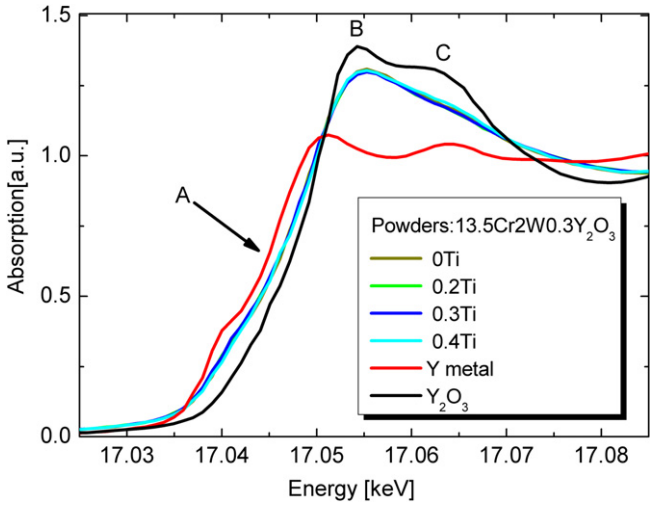

Fig. 2. Y K-edge XANES spectra of the powder samples after MA together with the reference samples, metal Y and Y_2O_3, the absorption edge, the main peak and the shoulder at the post edge are marked by A, B and C, respectively.

3.2.2. Compacted samples

XANES spectra for the compacted samples are plotted in Fig. 4. In contrast to the milled powders, the chemical shifts (marked by the arrow A) of the compacted samples are very close to Y_2O_3. A linear fit as employed for the steel powder samples does not give satisfying results. This implies that the dissolved Y and other alloying elements (Ti) reprecipitate from the steel during HIP. The compacted sample with 0.3% Ti exhibits the highest absorption peak B. And the 0.4% Ti sample shows an increased intensity in shoulder C, which suggests the presence of new Y oxide phases.

3.3. EXAFS

3.3.1. Powders

The Fourier transform (FT) of the EXAFS functions of the powder samples and two references are shown in Fig. 5. The primary feature of Fig. 5 is two dominant peaks for pure Y_2O_3, which are assigned to the Y–O and Y–Y coordination shells. The first Y–Y shell in the Y metal has a larger R than that for the second Y–Y shell in the Y_2O_3. The MA powders are characterized by two similar peaks, close to Y_2O_3. The much smaller peak height of the Y–Y indicates that the Y_2O_3 in the MA powders is much more disordered because of severe plastic deformation. The small portion of metallic Y component is invisible because of their overlap with the second Y–Y shell of Y_2O_3. No evident difference is observed for the MA powders with differing amounts of Ti.

Table 2
Relative fraction of the metallic Y component in the MA powders determined from the linear fit of XANES.

Composition	0Ti	0.2Ti	0.3Ti	0.4Ti
%	10.2	12.8	13.7	11.5

Fig. 6 presents the theoretical fitting of the first two shells using the phaseshift and backscattering amplitude extracted from the crystallographic structure of cubic Y_2O_3. The reasonable fitting results for all the powder samples are listed in Table 3. The local structure of cubic Y_2O_3 can be divided into three shells: Y–O with $R = 2.26$ Å, Y–Y1 with $R = 3.50$–3.53 Å, and Y–Y2 with $R = 4.04$–4.09 Å. The similarity of the FTs of the pure Y_2O_3 and the MA powders indicates that Y_2O_3 is the main constituent of Y even after 24 h milling, which is consistent with the results of the XANES. However, the yttrium oxides after the MA are different from the initially added Y_2O_3 powders, with a decreased coordination number, especially for the second Y–Y shell. This can be explained by severe plastic deformation introduced by the high energy MA. Large plastic deformation results in the generation of a stacking of various structural defects and refined crystallites, which destabilizes the ordered lattice and lead to the formation of more disordered (crystalline or amorphous) phases. It should be added that the fitted Y–Y1 shell may also contain a Y metallic component.

3.3.2. Compacted samples

The Fourier transform of the EXAFS data for the compacted ODS samples is shown in Fig. 7. After HIP, the local structure of Y shows a distinctive feature of Y oxides, but varying from one to another. It is noteworthy that different contents of Ti remarkably affect the local structure of Y. The sample with 0.3% Ti shows the largest Y–O peak. The Y–Y shell for the sample with 0% Ti splits into two peaks, whereas the samples containing Ti exhibit Y–Y shells similar to yttria.

In order to quantitatively interpret the trends observed in the FT, the first two peaks were fitted independently for the compacted samples. For the Ti-free compacted sample, the model Y_2O_3 did not have a good fit. Therefore, a new fitting model was selected with the complementary results obtained by TEM. An HRTEM study revealed the presence of cubic Y_2O_3 in the HIPed EUROFER-ODS alloy without Ti [5]. In spite of a relatively higher Gibbs energy of formation compared to Y_2O_3, a ternary oxide $YCrO_3$ coexists with Y_2O_3 in Fe–12Cr–0.4Y_2O_3 alloy after HIP and annealing [16]. Therefore, $YCrO_3$ was chosen as the model compound for EXAFS

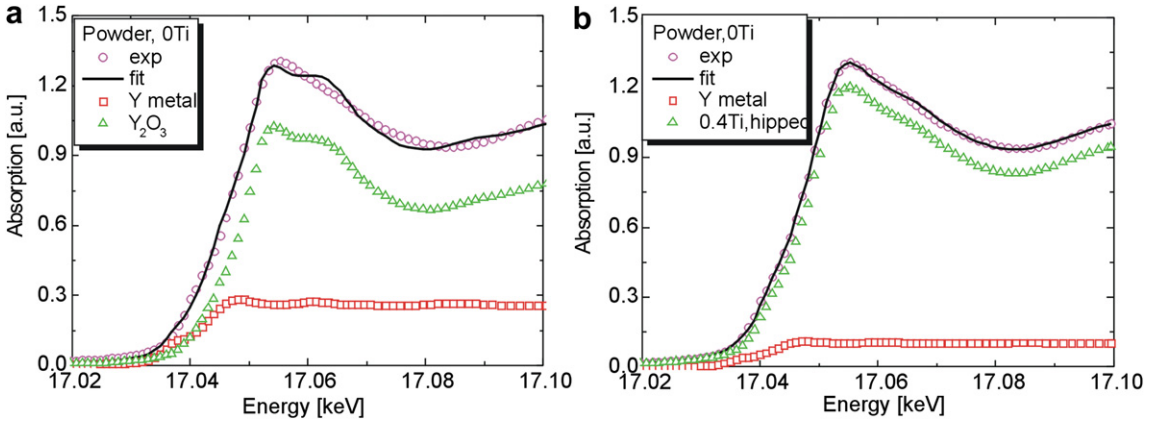

Fig. 3. Y K-edge XANES of MA powders (0 wt. % Ti) and a linear fit by (a) Y metal and Y_2O_3, (b) by Y metal and compacted sample with 0.4 wt. % Ti.

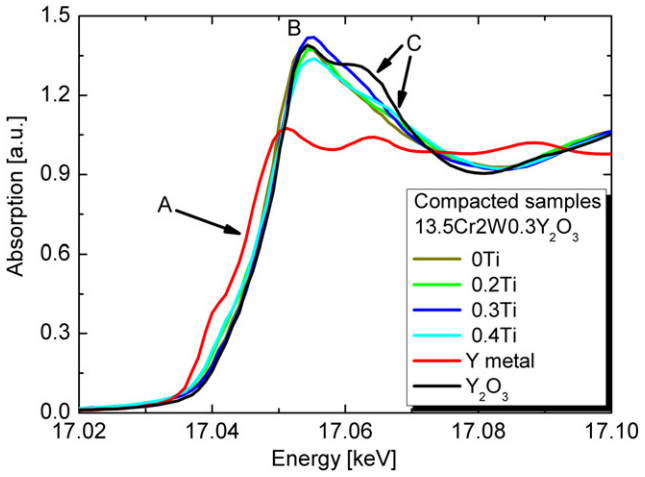

Fig. 4. Y K-edge XANES of the compacted samples and the reference samples, Y and Y_2O_3, the absorption edge, the main peak and the shoulder at the post edge are marked by A, B and C, respectively.

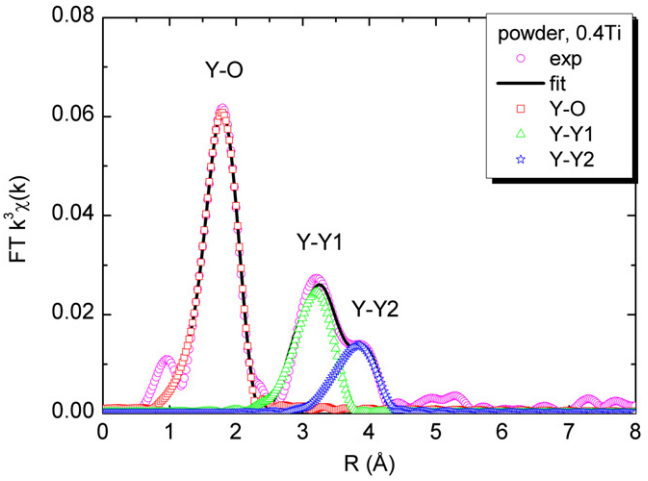

Fig. 6. Fourier transform of EXAFS functions of MA powders with 0.4% Ti and fitting with three coordinations: Y–O, Y–Y1 and Y–Y2. Phaseshift was not corrected.

fitting for the Ti-free ODS sample. Y_2TiO_5 and $Y_2Ti_2O_7$ [6] were considered for the − ODS samples containing Ti. The local structural parameters of some model compounds are listed in Table 4.

The interatomic distance R and the merit-of-fit with a model compound can be used for the identification of scattering atom species around a Y absorber. The fitting parameters for all compacted ODS samples are summarized in Table 5. Moreover, Fourier transform of EXAFS functions and data fitting of Ti free compacted ODS sample is shown in Fig. 8. On the basis of the model $YCrO_3$, the first three coordination shells around the central Y absorber were fitted by Y–O, Y–Cr, and Y–Y coordinations, respectively. The first shell has an R of 2.28 Å, corresponding to a Y–O shell. The second shell, with an R of 3.22 Å, is likely to be either the Y–Fe shell with an R of 3.21 Å in $YFeO_3$ or the Y–Cr shell with an R of 3.19 Å in $YCrO_3$. The short distance excludes the possibility of Y–Y as in Y_2O_3. Based on the TEM observation which will be addressed later, the $YCrO_3$ model was used here. However, the R of the third shell, 4.01 Å, is larger than that in $YCrO_3$ (3.83 Å) but close to the R of 4.00 Å in cubic Y_2O_3, indicating a complex local structure due to a mixture of several species or the influence of the scatter O. The CN of Y–O shell (7.1) is larger than the nanoscale Y_2O_3 particles in the powder samples and the cubic Y_2O_3 (6), but consistent with the $YCrO_3$ model.

The compacted samples containing Ti have only two characteristic peaks in the FT (shown in Fig. 7). The third peak is not distinct, making it difficult to specify which nano phases, Y_2O_3 or Y–Ti–O, exist. The alloy with 0.3% Ti seems to be consistent with Y_2O_3 with $R_{Y\text{-}O} = 2.27$ Å and $R_{Y\text{-}Y} = 3.53$ Å, but the high CN (8.5) of the first Y–O shell indicates that this is not a simple cubic Y_2O_3. As reported in the literature [17], a highly defected cubic phase Y_2O_3 with a space group Fm3m may form, the CN of the Y–O shell is 8, but the second shell of this phase with a R of 3.72 Å is much larger than that of 3.53 Å in the 0.3% Ti sample. Other compacted samples cannot be clearly identified as any of the single phases of the known Y–O and Y–Ti–O phases as mentioned above. It is likely that Y forms a mixture of various species, and none of them are dominant. As a spectroscopic technique, XAFS probes only an average over all species. The coordination peaks at high order shells are rather dispersed even for the compacted samples after HIP and annealing.

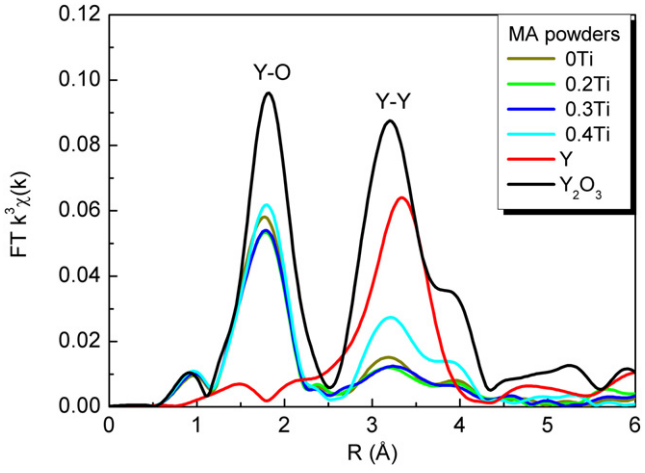

Fig. 5. Fourier transform of EXAFS functions of MA steel powders and metal Y, Y_2O_3 references, phaseshift was not corrected. The two peaks corresponding to Y–O and Y–Y are marked.

3.4. TEM

TEM techniques are powerful tools for the investigation of second-phase precipitates by providing direct evidence of chemical composition and crystal structure of individual particles. The second-phase precipitates observed in these compacted ODS steels have been discussed in our previous work [9]. Briefly, they can be divided into two classes: a small density of large inclusions with

Table 3
Fitted results[a] of Y–O, Y–Y1, Y–Y2 shells for MA powders. The σ^2 for Y–Y1 and Y–Y2 were fixed. The data for c-Y_2O_3 were taken from the literature [22].

		c-Y_2O_3	0Ti	0.2Ti	0.3Ti	0.4Ti
Y–O	R(Å)	2.27	2.26	2.26	2.26	2.26
	CN	6	5.5	5.4	5.4	5.4
	σ^2	–	0.0089	0.0095	0.0094	0.0081
Y–Y1	R	3.52	3.52	3.5	3.52	3.53
	CN	6	1.9	1.5	1.5	3.4
	σ^2	–	0.01	0.01	0.01	0.01
Y–Y2	R	4.01	4.09	4.08	4.04	4.06
	CN	6	1.7	1.6	1.6	2.9
	σ^2	–	0.01	0.01	0.01	0.01

[a] The fitting results for MA powder samples in Table 3 include the average coordination number (CN), bond length (R) and relative Debye–Waller factor (σ^2) at different coordination shells.

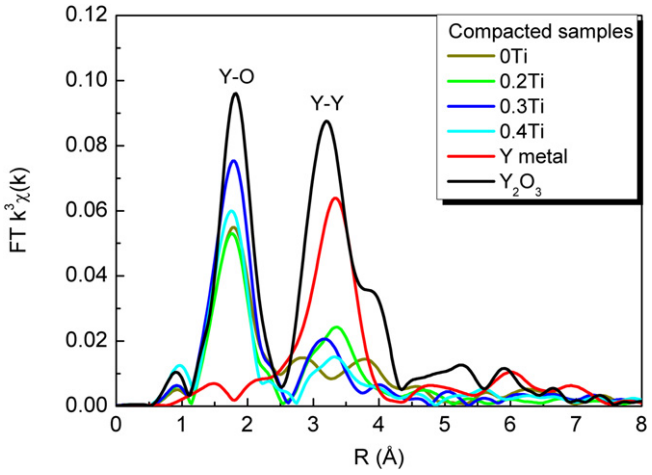

Fig. 7. Fourier transform of EXAFS functions of compacted ODS samples with metal Y and Y_2O_3 references.

sizes up to 1 μm and a large population of nanoscale particles with an average particle size <10 nm. Currently, the EDX elemental maps shown below are excellent complement to the XAFS results. For the 0% Ti alloy, the inclusions are visible as round spots on Fig. 9a, with a contrast similar to that of the matrix. Elemental mapping of Fe (Fig. 9b) clearly reveals regions of local Fe deficiency owing to the superior signal/noise ratio. The O image (Fig. 9c) exhibits patterns of local O enrichment which perfectly correlate with the Fe deficiency map. On the Y element map, only several ODS particles can be detected, which are marked with red circles. These findings suggest the coexistence of Cr oxides and Y–Cr–O particles. However, the Cr–O/Y–Cr–O complex oxides are occasionally observed in the 0% Ti alloy and coarse Cr oxides exhibit a much smaller number density and volume fraction compared to Y oxides. A similar complex oxide structure of γ-Al_2O_3/Y–Al–O has been observed in Al-containing alloy PM 2000 [18].

Relatively high values of $R_{Y\text{-}Y}$ in 0.2Ti and 0.4Ti alloys indicate the formation of new nano phases rather than continuity of the original yttria phase. The HAADF image of these particles is shown in Fig. 10a. The particles (indicated by green arrows) located at a grain boundary (indicated by red dashed lines) have a larger size, which is likely detectable. All these particles with Fe and Cr deficiency are imaged as dark spots on the Fe (Fig. 10b) and Cr (Fig. 10c) maps. The spatial distributions of Ti and Y on the elemental maps (Fig. 10d and e) are in good agreement with Fe and Cr deficiency. The EDX elemental mapping clearly reveals the presence of Y–Ti–O oxide. However, it cannot exclude the existence of Y_2O_3 in Ti-containing ODS alloys.

4. Discussion

4.1. Evaluation of XAFS for the study of ODS steels

Over the past 30 years, XAFS has been successfully applied to a wide range of scientific fields due to the rapid development of synchrotron sources [19,20]. However, very little XAFS research has been conducted for ODS alloys. The application of the XAFS technique to ODS alloys is evaluated as follows:

(1) XAFS is element specific, so one can focus on one specific element without interference from the other elements present in the sample. (2) High brilliant third generation synchrotron radiation provides the opportunity for the study of dilute samples. XAFS measurements can be made on elements of minor and even trace contents (down to several ppm). The addition of Y_2O_3 in ODS steels is mainly between 0.2% and 0.5% (wt. %). A recent study [21] has successfully demonstrated the characterization of precipitations in two ODS steels by a complementary application of XAFS and XRD using synchrotron irradiation sources. (3) XAFS is an atomic probe and is not limited by the state of the sample. Importantly, crystallinity is not required. It is only sensitive to the local structure of the absorbing atoms, which makes it one of the few powerful tools available for noncrystalline and highly disordered materials. (4) There are no strict requirements for the shape and the size of the specimen. Compared with TEM, no vacuum is required, specimens are easy to make and no artifacts are introduced during sample preparation. A large beam size allows the measurement of a large illuminated area so that the adverse influence of the microstructural heterogeneity in ODS alloys can be eliminated.

However, the limitations are (1) though the measurement of XAFS is simple, a comprehensive understanding of the results involves a combination of modern physics, chemistry, materials science, and a complete mastery of data analysis. (2) Since XAFS provides only indirect evidence about the speciation of oxide phases, other techniques such as TEM or XRD are always essential to make an accurate determination. (3) A very long cycle and the relatively poor availability of synchrotron radiation beamtime is an important restraint.

4.2. Evolution of Y_2O_3 during the fabrication process

MA is a critical step in studying the formation mechanism of nanoscale second-phase oxides. Numerous variables, such as the type of the mill [22], milling time [21,23], mill speed, and milling atmosphere [24] have been extensively investigated. The mean particle size extracted from XRD data has been used to determine the optimum milling time in previous studies [21,23]. The

Table 5
The fitting results and experimental data for compacted ODS samples. (a) Ti free sample. (b) Ti-containing samples.

Y K-edge	Y–O			Y–Cr			Y–Y		
	CN	*R*	σ^2	CN	*R*	σ^2	CN	*R*	σ^2
0 Ti	7.1	2.28	0.012	2.1	3.22	0.011	9.1	4.01	0.019

Y K-edge	Y–O			Y–Y		
	CN	*R*	σ^2	CN	*R*	σ^2
0.2Ti	6.5	2.27	0.0081	3.5	3.60	0.010
0.3Ti	8.5	2.27	0.0109	5.3	3.53	0.0146
0.4Ti	5.9	2.24	0.0093	2.2	3.62	0.010

Table 4
Local structures around Y of some Y oxide compounds, including the coordination number, interatomic distance (Å) of each shell and space group.

Compound	First shell	Second shell	Third shell	Crystal structure	Space group	Reference
Y_2O_3	6O(2.28Å)	6Y(3.52Å)	6Y(4.00Å)	Cubic	Ia-3	[22]
$YCrO_3$	8O(2.41Å)	6Cr(3.19Å)	6Y(3.83Å)	Orthorhombic	Pbnm	[24]
$YFeO_3$	8O(2.43Å)	6Fe(3.21Å)	6Y(3.86Å)	Orthorhombic	Pnma	[25]
Y_2TiO_5	7O(2.34Å)	4Ti(3.54Å) 3Ti(3.45Å)		Orthorhombic	Pnma	[26]
$Y_2Ti_2O_7$	8O(2.43Å)	6Ti(3.57Å)	6Y(3.57Å)	Cubic	Fd-3m	[27]

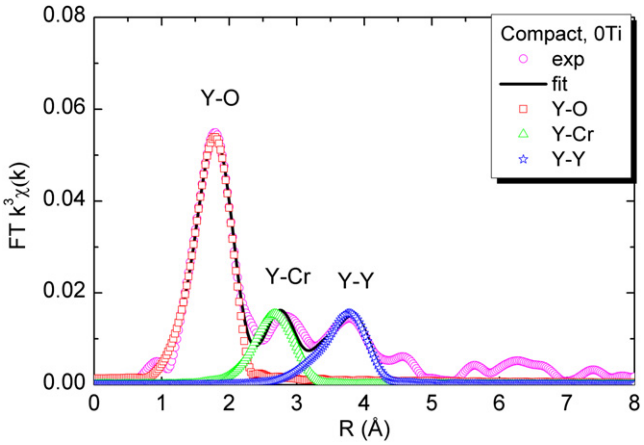

Fig. 8. Fourier transform of EXAFS functions of 0% Ti compacted sample and data fit employing three coordinations: Y–O, Y–Cr and Y–Y. Phaseshift was not corrected.

microstructure has been observed in most cases by SEM together with EDX. The spatial resolution of EDX in a SEM does not allow a reliable mapping of the distribution of Y. Very little TEM work has been performed on the MA ODS steel powders due to the challenging sample preparation required. A new approach [25] for TEM sample preparation of MA powders has been demonstrated recently. It was found that the dissolution of Y_2O_3 is strongly dependent on the milling time. The complete dissolution of Y_2O_3 is observed after 80 h milling with a speed of 1200 rpm. In this work, XAFS has revealed that only 10%–14% of the initially added 0.3 wt. % Y_2O_3 dissolved into the steel matrix after 24 h milling with the same milling machine and ball-to-powder ratio. This suggests that long-term milling is required for the complete dissolution of Y_2O_3. However, careful control of the enhanced contamination of undesired impurities such as O, N and C with increased milling time is required.

Unlike the initial Y_2O_3 (Fig. 4), the undissolved Y_2O_3 shows highly disordered structures resulting from severe plastic deformation during the MA. Y-enriched oxides in compacted ODS steels are more dispersed than pure Y_2O_3. This suggests the coexistence of crystalline nanoparticles and disordered phases after high temperature consolidation and annealing. Both crystalline nanoparticles larger than 2 nm and amorphous (or disordered) cluster domains smaller than 2 nm have been observed in MA956 and Fe-16Cr-4.5Al ODS steels by HRTEM. The amorphous nanoclusters are supposed to play an important role in enhancing the radiation resistance of ODS steels with respect to helium management [26]. Small angle neutron scattering (SANS) has been used to evaluate the average radius (r), number density (N), and volume fraction (f) of these ultrafine nanoclusters. SANS shows that MA957 and J12YWT contain NFs with $r = 1.3$ nm and 1.6 nm, $N = 6.6 \times 10^{23}$ m^{-3} and 3.9×10^{23} m^{-3}, and $f = 0.65\%$ and 0.69%, respectively [21]. This could explain why it is difficult to get a good fit for XAFS with any known Y–O or Y–Ti–O phase.

Furthermore, the interaction of Ti and Y_2O_3 in ODS steels is the focus of related research. The addition of an appropriate amount of Ti is beneficial to refine the particle size and increase the particle number density, which leads to outstanding tensile and creep properties. However, it should be emphasized that coarse TiO_2 occurs when the excess oxygen concentration is too high. Several attempts have been made to eliminate or minimize the unfavorable brittle phase. In the present study, the addition of TiH_2 powders rather than pure Ti powder can, to a great extent, avoid Ti oxidation and reduce the concentration of excess oxygen during fabrication process. It is also confirmed that slight variations of Ti content in the range from 0.2% to 0.4% lead to obvious particle size refinement

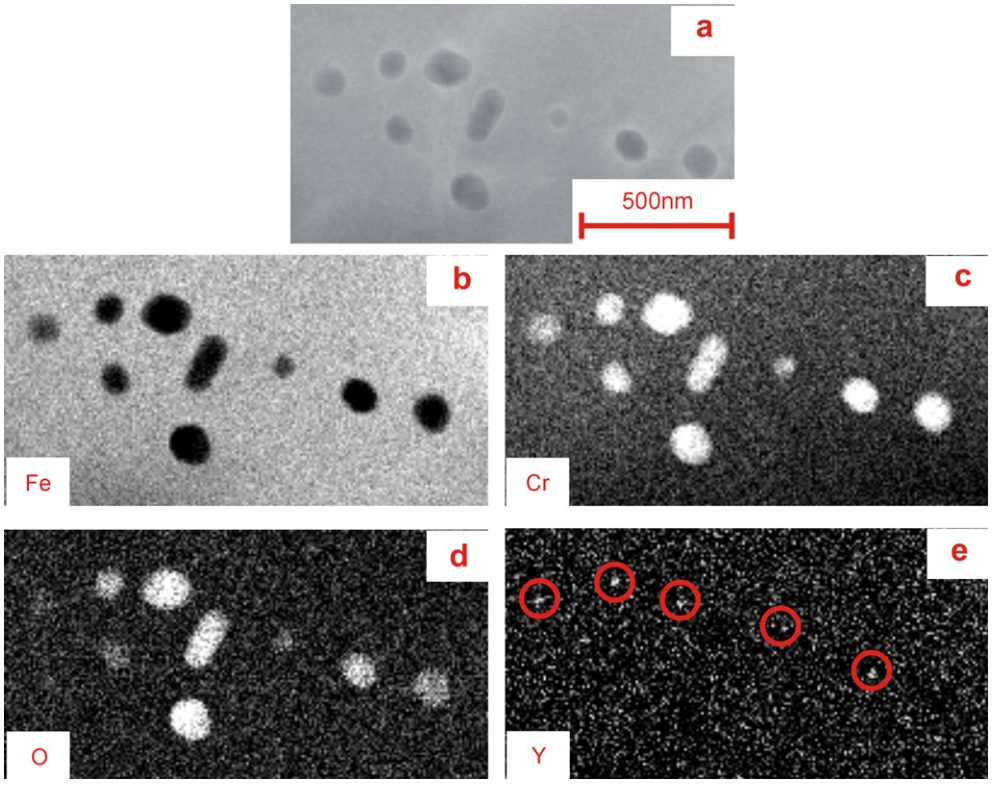

Fig. 9. (a) HAADF image and EDX elemental distribution maps (b) Fe, (c) Cr, (d) O and (e) Y of Cr–O/Y–Cr–O particles in 0% Ti ODS alloy.

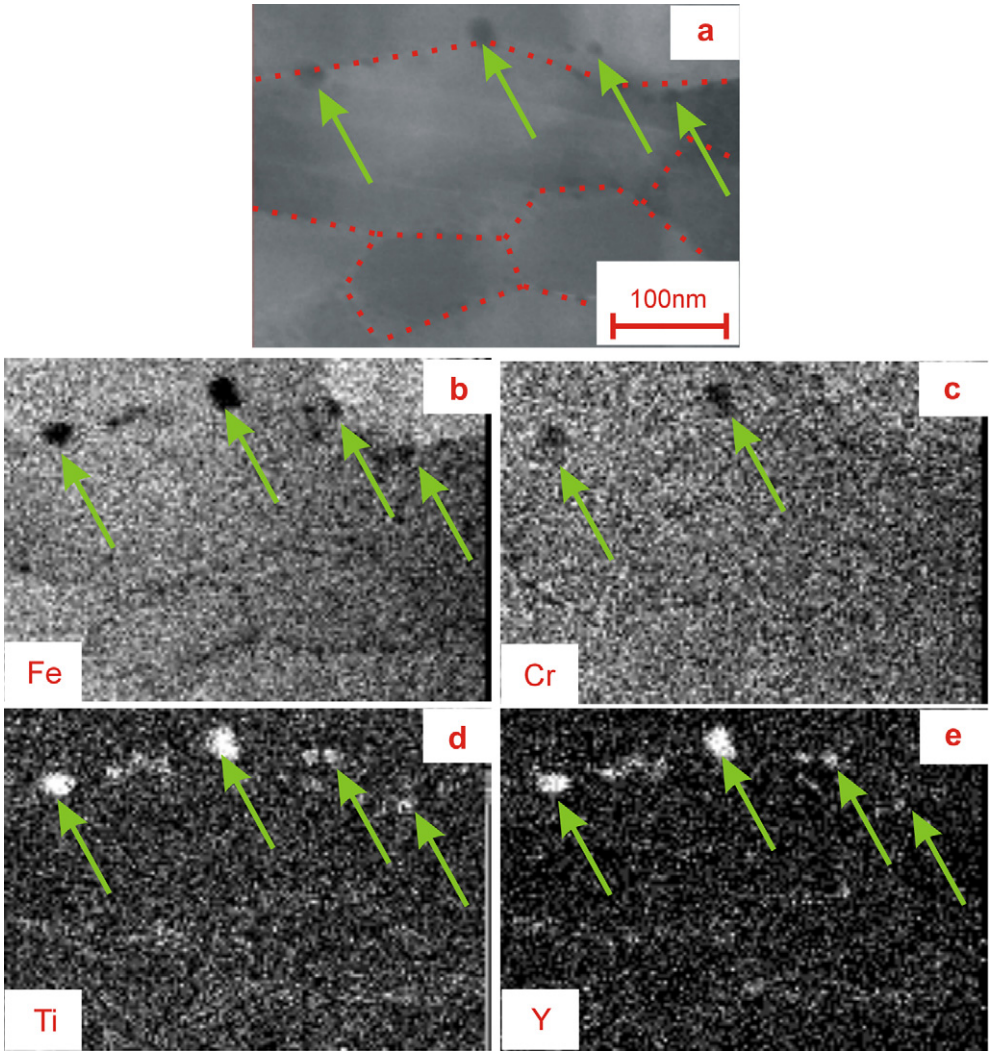

Fig. 10. (a) HAADF image and EDX elemental distribution maps (b) Fe, (c) Cr, (d) Ti and (e) Y of Y–Ti–O particles in 0.4% Ti ODS alloy.

and the optimum is achieved by adding 0.3% Ti [9]. The XAFS and TEM results indicate that Ti addition influence not only the morphology but also the chemistry of the nanoscale particles.

5. Conclusions

The speciation and local structures of Y oxide in several ODS alloys have been studied by a joint combination of XAFS and TEM. The samples for the investigation included ODS steel powders after MA and compacted bulk samples after HIP and annealing. The following conclusions have been drawn:

(1) XAFS provides a non-destructive way to study the physical and chemical state of dilute species in ODS alloys. It enables the study of Y-enriched nanoparticles with a low concentration (usually 0.2%–0.5%) by measuring Y K-edge XAFS. The XAFS reveals the average structural information and the dominant species, which is complementary to the knowledge of the individual particles obtained by TEM.
(2) A linear combination fit of the XANES enables a quantitative determination of $Y_{dissolved}/Y_{total}$ for milled powders. After 24 h of milling, 10%–14% of the initially added 0.3 wt. % Y_2O_3 dissolves into the steel matrix. The varied Ti contents exhibit a minor influence on Y solid solution during the MA.
(3) After HIP and annealing, similar XANES spectra have been obtained for 0%–0.4% Ti ODS alloys. The difference between the initial Y_2O_3 and the compacted ODS alloys at the Y K-edge suggests the formation of new nano phases during the HIP.
(4) Fitting of the EXAFS indicates the coexistence of Y_2O_3 and $YCrO_3$ in the Ti-free compacted ODS sample. EDX elemental mapping confirms the presence of complex oxides Y–Cr–O/Cr–O and shows local Fe deficiency at the precipitates.
(5) For – ODS alloys containing Ti, the dispersed high-order shells in the FT make it difficult to distinguish Y_2O_3 and Y–Ti–O species, in other words, none of them are dominant. EDX clearly reveals the presence of Y–Ti–O oxides at the grain boundary. The more dispersed Y-enriched oxides in the compacted ODS steels indicate the coexistence of crystalline nanoparticles and disordered phases after high temperature consolidation and annealing.

Acknowledgments

The authors acknowledge financial and technical support from the China Scholarship council (CSC), the European Community under the contract of Association between EURATOM and the Karlsruhe Institute of Technology and the European Synchrotron Radiation Facility (ESRF). This work was carried out within the

framework of the European Fusion Development Agreement. The views and opinions expressed herein do not necessarily reflect those of the European Commission.

References

[1] A. Hirata, T. Fujita, Y.R. Wen, J.H. Schneibel, C.T. Liu, M.W. Chen, Nat. Mater. 10 (2011) 922–926.
[2] S. Yamashita, N. Akasaka, S. Ukai, S. Ohnuki, J. Nucl. Mater. 367–370 (2007) 202–207.
[3] A. Moeslang, C. Adelhelm, R. Heidinger, Int. J. Mater. Res. 99 (2008) 1045–1054.
[4] S. Ukai, M. Harada, H. Okada, M. Inoue, S. Nomura, S. Shikakura, K. Asabe, T. Nishida, M. Fujiwara, J. Nucl. Mater. 204 (1993) 65–73.
[5] M. Klimiankou, R. Lindau, A. Möslang, J. Cryst. Growth 249 (2003) 381–387.
[6] H. Sakasegawa, L. Chaffron, F. Legendre, L. Boulanger, T. Cozzika, M. Brocq, Y. de Carlan, J. Nucl. Mater. 384 (2009) 115–118.
[7] M.K. Miller, D.T. Hoelzer, E.A. Kenik, K.F. Russell, J. Nucl. Mater. 329–333 (2004) 338–341.
[8] M.K. Miller, K.F. Russell, D.T. Hoelzer, J. Nucl. Mater. 351 (2006) 261–268.
[9] P. He, M. Klimenkov, R. Lindau, A. Möslang, J. Nucl. Mater. 428 (2012) 131–138.
[10] T. Ressler, J. Phys. IV France 7 (1997) C2-269–C262-C270.
[11] D.C. Koningsberger, B.L. Mojet, G.E. van Dorssen, D.E. Ramaker, Top. Catal. 10 (2000) 143–155.
[12] V. Swamy, H.J. Seifert, F. Aldinger, J. Alloys Compd. 269 (1998) 201–207.
[13] B. Guo, Z.-P. Luo, J. Am. Ceram. Soc. 91 (2008) 1653–1658.
[14] C. Degueldre, S. Conradson, W. Hoffelner, Comput. Mater. Sci. 33 (2005) 3–12.
[15] T. Liu, H. Xu, W.S. Chin, P. Yang, Z. Yong, A.T.S. Wee, J. Phys. Chem. C 112 (2008) 13410–13418.
[16] V. de Castro, E.A. Marquis, S. Lozano-Perez, R. Pareja, M.L. Jenkins, Acta Mater. 59 (2011) 3927–3936.
[17] S. Katagiri, N. Ishizawa, F. Marumo, Powder Diffr. 8 (1993) 60.
[18] M. Klimiankou, R. Lindau, A. Möslang, J. Schröder, Powder Metall. 48 (2005) 277–287.
[19] J.M. Corker, J. Evans, J.M. Rummey, Mater. Chem. Phys. 29 (1991) 201–209.
[20] M. Di Vece, A.M.J. van der Eerden, D. Grandjean, R.J. Westerwaal, W. Lohstroh, S.G. Nikitenko, J.J. Kelly, D.C. Koningsberger, Mater. Chem. Phys. 91 (2005) 1–9.
[21] N.Y. Iwata, A. Kimura, M. Fujiwara, N. Kawashima, J. Nucl. Mater. 367–370 (2007) 191–195.
[22] M.J. Alinger, G.R. Odette, D.T. Hoelzer, Acta Mater. 57 (2009) 392–406.
[23] A. Ramar, Z. Oksiuta, N. Baluc, R. Schäublin, Fusion Eng. Des. 82 (2007) 2543–2549.
[24] Z. Oksiuta, N. Baluc, J. Nucl. Mater. 386–388 (2009) 426–429.
[25] J. Hoffmann, M. Klimenkov, R. Lindau, M. Rieth, J. Nucl. Mater. (2011). http://dx.doi.org/10.1016/j.jnucmat.1034, 2011.1009.
[26] L.L. Hsiung, M.J. Fluss, S.J. Tumey, B.W. Choi, Y. Serruys, F. Willaime, A. Kimura, Phys. Rev. B: Condens. Matter 82 (2010) 184103.
[27] E. Chtoun, L. Hanebali, P. Garnier, J.M. Kiat, Eur. J. Solid State Inorg. Chem. 34 (1997) 553.